Journal of Applied Physics

Solar-active titanium-based oxide photocatalysts loaded on TiN array absorbers for enhanced broadband photocurrent generation

Cite as: J. Appl. Phys. **129**, 023103 (2021); https://doi.org/10.1063/5.0031400
Submitted: 30 September 2020 . Accepted: 21 December 2020 . Published Online: 11 January 2021

Satish Laxman Shinde, Hai Dang Ngo, Thien Duc Ngo, Satoshi Ishii, and Tadaaki Nagao

Journal of Applied Physics ARTICLE scitation.org/journal/jap

Solar-active titanium-based oxide photocatalysts loaded on TiN array absorbers for enhanced broadband photocurrent generation

Cite as: J. Appl. Phys. **129**, 023103 (2021); doi: 10.1063/5.0031400
Submitted: 30 September 2020 · Accepted: 21 December 2020 ·
Published Online: 11 January 2021

Satish Laxman Shinde,[1,a)] Hai Dang Ngo,[1,2] Thien Duc Ngo,[1,2] Satoshi Ishii,[1] and Tadaaki Nagao[1,2,a)]

AFFILIATIONS

[1]International Center for Materials Nanoarchitectonics, National Institute for Materials Science, Tsukuba, 305-0044, Japan
[2]Department of Condensed Matter Physics, Hokkaido University, Sapporo, 060-0808, Japan

Note: This paper is part of the Special Topic on Hot Electron Physics and Applications.
[a)]**Authors to whom correspondence should be addressed:** NAGAO.Tadaaki@nims.go.jp and SHINDE.Satishlaxman@nims.go.jp

ABSTRACT

Efficient utilization of a wide range of the solar spectrum in photoelectrochemical conversion is one of the primary requirements for photocatalyst materials. Here, we report an effective approach to combine solar-absorptive titanate-based oxide photocatalysts with titanium nitride (TiN) to demonstrate the enhanced photocurrent generation extending from the ultraviolet to the near-infrared region. Pseudobrookite Fe_2TiO_5 and Cr-doped TiO_2 are, respectively, loaded on the TiN nanodisk arrays to demonstrate the photocurrent generation in opposite directions. By incorporating the TiN nanodisk arrays, the photocatalytic performance of Fe_2TiO_5 has increased by 26-fold in the UV region and ~11-fold in the visible region due to the strong UV–visible light absorption, hot electron generation at the TiN nanodisk array, and their subsequent injection into the oxide. Similarly, the photocatalytic performance of Cr-TiO_2 has increased by ~18-fold in the UV region and ~sixfold in the visible region by the hot hole transfer from TiN. This work demonstrates the effective utilization of titanium-based catalysts activated with both hot-electrons and holes from the TiN, yielding the visible-photocurrent generation and thus the improved photon management in solar photocatalysis.

I. INTRODUCTION

Semiconductor photocatalysts are widely studied for converting sunlight into electricity or fuels.[1–4] In the past few decades, a variety of solar light-active semiconductor photocatalysts have been developed.[5–12] Among these, hematite (Fe_2O_3) has drawn intensive attention as photocatalyst materials because of its bandgap (2.1–2.2 eV) favorable for visible absorption, chemical stability, and earth abundance.[9,13,14] However, its poor conductivity, short charge carrier diffusion length, indirect bandgap, and poor oxygen evolution reaction kinetics make it inferior compared to commonly used TiO_2, which has higher carrier mobility as well as chemical/mechanical robustness.[14] Recently, pseudobrookite Fe_2TiO_5, which assumes the feature in between TiO_2 and Fe_2O_3, has been recognized as a promising material for visible photocatalysts because of its suitable band edge positions and appropriate atomic structures to realize both the water oxidation reaction and the fast charge separation/transfer at the electrode/electrolyte interface.[7,15–17] Its short charge carrier diffusion length suggests that it is advantageous to use in the form of thin films; however, little was known on the film growth of this material until recently. Also, when used in the form of thin film, it faces the difficulty of small photon absorption due to the short optical path length of the material. Recently, the problem of thin film growth was overcome by adopting an appropriate condition of sputter deposition. Regarding weak optical absorption, several efforts have been made to overcome this problem including doping, integration with other oxides, and resonant oxide nanostructures, but yet with limited success.[18–20] In this context, combining oxide semiconductors with metal nano-absorbers is known to improve the solar light absorption and increase solar energy conversion efficiency.[8,21–25] The light-matter interaction is greatly enhanced by light nanofocusing effect as well as increased optical path length via light scattering. Furthermore, hot carrier transfer through the metal interface to a nearby object,

such as a molecule or a semiconductor, can boost their photocatalytic performance.[8,21–25] Noble metals such as Ag and Au have been adopted so far, but their effective spectral bands are rather narrow and a strong quest exists for the broader spectral band that is compatible to the broad solar spectrum.

Titanium nitride (TiN), which is a conductive ceramic, has a strong and broadband optical response from the visible to near-infrared (NIR) region, also exhibiting a plasmonic response above ~500 nm, has emerged as an ideal material for solar photoenergy applications. It exhibits strong metallicity and behaves as an effective "hot carrier generator" in the visible and NIR region.[26–29] The material can be used to enhance the photocatalytic activity in the visible–NIR region[30,31] and to extend the detection wavelength of semiconductor photodetectors.[32,33] Similar to gold or silver, both hot electrons and hot holes excited in TiN can be used, for instance, to increase the responsivities and detection wavelengths of photodetectors and to enhance photocatalytic performance. However, hot hole excitation in TiN is much less explored[34,35] compared to hot electron excitation in TiN and not discussed in comparison to hot electron excitation.[36–38] Therefore, it is worth studying hot hole transfers, as well as making a thorough comparison of hot electrons and hot holes from performance perspectives. To this end, in addition to Fe_2TiO_5, we chose chromium doped titania (Cr-TiO_2) as a p-type semiconductor to study hot hole excitation in TiN.

Here, we report broadband and strong solar light absorption by combining Fe_2TiO_5 or Cr-TiO_2 photocatalysts with TiN nanodisk arrays for photoelectrochemical (PEC) conversion. A colloidal nanosphere lithography combined with dry etching was used to fabricate the TiN nanodisk arrays. Compared to the bare Fe_2TiO_5 film, hybrid TiN/Fe_2TiO_5 nanodisk arrays showed ~26-fold improvement in the photoelectrochemical performance owing to the injection of hot electrons. Similarly, in the presence of TiN, photoelectrochemcial activity of the TiN/Cr-TiO_2 hybrid system reached ~18-fold because of the contribution of hot holes. Strong visible light absorption and hot carrier (electrons and holes) injection due to TiN nanodisk arrays enhanced the photocurrent generation in the oxide catalysts. The present approach of combining TiN nanodisk arrays with earth-abundant semiconductors is a promising strategy to develop efficient and stable photocatalytic nanosystems for water splitting.

II. EXPERIMENTS AND METHODS

Preparation of Fe_2TiO_5 thin film: The Fe_2TiO_5 thin films were deposited on ITO glass substrates by a magnetron sputtering system (i-Miller CFS-4EP-LL, Shibaura) using a commercially available Fe_2TiO_5 sputter target (Furuchi Chemical Co.). The detailed sputtering conditions are provided in Table S1 in the supplementary material. After the deposition, the Fe_2TiO_5 films were annealed in air at 550 °C for 1 h (quartz tube furnace, Koyo Thermo Systems) for further characterizations.

Preparation of Cr-TiO_2 thin film: A mixture of 5 ml of ethanol and 0.12 g of chromium nitrate ($Cr(NO_3)_3$) was vigorously stirred for 1 h at RT, and 2 ml of titanium (IV) butoxide (Ti[$O(CH_2)3CH3$]4). was added dropwise into the solution. A green solution was obtained. Furthermore, a mixture of 240 μl of water, 5 ml of ethanol, and 260 μl of HNO_3 was added dropwise to the initial solution. The resultant solution was spin coated on ITO substrates and after annealing in air, the Cr-TiO_2 thin films were obtained. The detailed procedure is reported elsewhere.[30]

Fabrication of TiN/Fe_2TiO_5 and Au/Fe_2TiO_5 samples: The samples were prepared by sputtering the 60-nm thick Fe_2TiO_5 film on either 200-nm thick TiN or Au films deposited on the ITO substrates.

Fabrication of TiN/Fe_2TiO_5 and TiN/Cr-TiO_5 nanodisk arrays: The TiN nanodisk arrays were fabricated by the combination of colloidal lithography and dry etching. Briefly, in the first step, 200 nm thick TiN films were deposited on 2×1 cm^2 ITO substrates via the magnetron sputtering system. The detailed condition for TiN film deposition is given in Table S1 in the supplementary material. In the second step, a close-packed monolayer of polystyrene (PS) nanospheres (500 nm in diameter, Thermo Fisher Scientific Inc.) was deposited on top of the TiN layer via colloidal self-assembly. The details of the self-assembly process and nanosphere lithography can be found in our previous reports.[39] The PS spheres acted as a mask to make nanodisk arrays. In the third step, O_2 plasma was used to shrink the size of the PS spheres (20 sccm, RF power 200 W, bias power 5 W, Ulvac CE-300I). In the fourth step, the Cl_2/BCl_3 plasma was used to etch the TiN layer with the same etching machine (4 sccm Cl_2/16 sccm BCl_3, RF power 200 W, bias power 20 W). In the fifth step, the PS spheres were then removed by sonicating the film in chloroform solution, and the TiN nanodisk arrays having 410 nm diameters on ITO substrate were fabricated. Finally, the 60 nm thick Fe_2TiO_5 thin film was deposited onto the nanodisk arrays via sputtering giving rise to hybrid nanodisk structures of ITO/TiN/Fe_2TiO_5. Similarly, using the sol-gel method, the 60 nm thick Cr-TiO_2 film was deposited on planar and nanodisk arrays of TiN (disk diameter 410 nm) to form the ITO/TiN/Cr-TiO_2.

Characterization and measurements: Scanning electron microscope (SEM) images of the samples were obtained using a Hitachi microscope (SU8230). The x-ray diffraction (XRD) pattern was measured by a Rigaku Ultima III, Rint 2000 instrument. The reflectance and permittivity of the films were measured using a UV−Vis spectrometer (V-570, Nihon Bunko) and a spectroscopic ellipsometer (SE 850, Sentech), respectively. The work function of the films were measured using Kelvin probe force microscopy (KPFM), which is based on an atomic force microscope (TT-2, AFM Workshop), combined with a surface potential measurement instrument (SPT-20, Toyo Corp.).

Photoelectrochemical measurements: The photocurrent was measured using a two-electrode system (Fig. S1 in the supplementary material) with a homemade reactor with a source meter (Keithley 2635A, Tektronix). In this system, a Pt wire was used as the counter electrode (CE), and the fabricated sample as the working electrode (WE). Na_2SO_4 (0.5 M) solution was used as an electrolyte for photocurrent measurements. The bias voltage was not applied during all the photocurrent measurements. To evaluate the wavelength-dependent incident photon-to-electron conversion efficiency (IPCE), a tunable wavelength light source (BUNKOUKEIKI, NIJI-2) with wavelength ranging from 350 to 750 nm was used. The measured photocurrent sign was opposite for Fe_2TiO_5 and Cr-TiO_2 samples. For comparison purposes, the negative photocurrent sign is changed

to positive. In the linear sweep voltammetry (LSV), the anodic photocurrent was measured using a potentiostat (VersaSTAT 4 Potentiostat Galvanostat) and a three-electrode system with a homemade reactor coupled with a quartz window. Ag/AgCl (saturated in KCl), Pt wire, and the fabricated sample were used as the reference electrode (RE), the counter and working electrode, respectively. Measurements were performed in 1 M NaOH (pH = 13.7) electrolyte under the irradiation from a solar simulator (XES-40S1, San-Ei Electric) with Air Mass value of 1.5 G (100 mW/cm^2).

Numerical simulations: The simulated absorptivities of the nanodisk arrays were calculated using the rigorous coupled-wave analysis (RCWA) (DiffractMOD, RSoft, Synopsys) and the electric field distribution were simulated with a full-wave simulation based on the finite-difference time-domain (FDTD) method (FullWAVE, RSoft Synopsys). The dielectric functions of the Fe_2TiO_5 and TiN films used in the simulations were retrieved from the spectroscopic ellipsometry measurements, and the dielectric function of Au was taken from the literature.[40] In the full-wave simulations, periodic boundary conditions were applied on both X and Y axes, and perfectly matched layers were applied on both directions of the Z axis; a grid size of 5 nm was chosen for all three axes. In the simulations, the excitation electromagnetic field propagated along the –Z axis and the electric field is polarized parallel to the X axis.

III. RESULTS AND DISCUSSIONS

Figure 1(a) shows the SEM image of the as-deposited and annealed Fe_2TiO_5 thin film. The surface of the films is continuous and contained different domains of small crystallites orienting in certain directions with nanoscale hills and valleys. The interface energy partly motivates for these preferential orientations of domains as well as the nanofacets.[41] The XRD patterns of the as-deposited and annealed film are shown in Fig. 1(b). All the major diffraction peaks are matched to the pseudobrookite phase of Fe_2TiO_5 (PDF No. 09-0182), confirming the successful physical deposition and the formation of the Fe_2TiO_5 phase. The peak at 51.6° is from the ITO substrate.[42]

The UV–Vis absorbance spectrum of the Fe_2TiO_5 thin film is shown in Fig. 1(c). To estimate the direct and indirect bandgaps of the Fe_2TiO_5 film, the Tauc plot was generated using absorbance spectra [Fig. 1(d)]. α, h, and ν are the absorption coefficient, Planck's constant, and photon energy, respectively. The direct and indirect bandgaps were estimated to be 3.2 and 1.9 eV, respectively, from the linear extrapolations to the energy axis. The Fe_2TiO_5 film shows strong absorption in the UV and visible (up to 570 nm) regions due to the direct (3.2 eV) and indirect (1.9 eV) bandgap transitions, respectively [Fig. 1(c)]. These direct and indirect bandgap optical transitions correspond to O 2*p*-Ti 3*d* and O 2*p*-Fe 3*d* transitions in Fe_2TiO_5.[41]

The wavelength-dependent dielectric function (optical permittivity) of Fe_2TiO_5 films was measured by a spectroscopic ellipsometer and used in the simulations for reflectance and absorptance calculations. The Tauc–Lorentz model was used to fit the permittivity. The real and imaginary parts of the permittivity are shown in Figs. 1(e) and 1(f), respectively. The imaginary part shows a strong peak in the UV and visible regions, related to the optical transitions between O 2*p* and Fe 3*d* bands and tails to up to 600 nm. The observed absorption properties of the Fe_2TiO_5 in the UV–visible region strongly support the promising features for application in the photochemical and photoelectric conversion. To further improve the absorption in the visible and NIR regions, the hybrid structures of plasmonic TiN and Fe_2TiO_5 were prepared in which the plasmonic TiN was supposed to enhance the photocatalytic performance of the Fe_2TiO_5 film.

Figure 2(a) shows the step-by-step fabrication process of hybrid nanodisk arrays where the details are given in the Experimental section. The well-defined nanodisk array of TiN on the ITO film is shown in Fig. 2(b). Figures 2(c) and 2(d) show the SEM images of nanodisk arrays after Fe_2TiO_5 and Cr-TiO_2 thin film deposition, respectively. The fabrication techniques used here are all scalable and multiple large-area samples with tunable size and shape of nanostructures can be produced simultaneously. It is noted that the TiN nanodisk arrays fabricated here can be readily combined with other photocatalytic materials, making this fabrication procedure attractive for various light-harvesting applications.

The measured and calculated absorptance of the planar and nanodisk array of the TiN film is shown in Fig. S2(a) in the supplementary material. The planar TiN film shows dielectric nature and exhibits broad absorption in the visible region, and the nanodisk array shows enhanced visible light absorption mainly due to the discontinuation of the TiN film. The plasmon enhanced absorption appears in the NIR, which can be seen in Fig. S2(b) in the supplementary material. Also, the absorptivity changes remarkably when the period of TiN disks (the disk diameter is 410 nm and the height is 200 nm) changes [Fig. S2(b) in the supplementary material] owing to diffraction. To provide insights into the electric field distributions at the nanodisk array, the simulated electric field maps of the TiN disk array at 900 nm excitation wavelength with a periodicity of 500 nm are presented in Fig. S2(c) in the supplementary material. This clearly confirms the laterally polarized nature of the disks and also displays the enhanced near-fields around the nanodisk surface. Thus, the plasmonic–photonic hybrid modes and near-field enhancement at the surface enhance the absorption of the TiN nanodisk arrays in the visible and NIR regions.

Figure 3(a) shows the measured and calculated absorptance spectra of planar ITO/Fe_2TiO_5, ITO/TiN/Fe_2TiO_5, and nanodisk arrays of ITO/TiN and ITO/TiN/Fe_2TiO_5 samples. As Fe_2TiO_5 has strong absorption in the UV region [Fig. 3(a)] and the TiN film has broad absorption in the visible region [Fig. S2(a) in the supplementary material], the planar ITO/TiN/Fe_2TiO_5 sample shows broad and enhanced absorption in the UV and visible regions. This broad absorption was further enhanced for the nanodisk array sample owing to the impedance matching and the localized surface plasmon resonances of the TiN nanodisks in the NIR. For ITO/TiN/Fe_2TiO_5 sample, the absorptivity can be optimized with the disk periodicity [Fig. 3(b)], and the strong electric field enhancement can be confirmed at the surfaces of the disks at the 900 nm excitation wavelength [Fig. 3(c)]. The simulated absorptance is in good agreement with experimental absorptance spectra. A little variation in the absorptance spectra between the experiments and simulations is likely to be caused by the deviation in the nanodisk morphology and

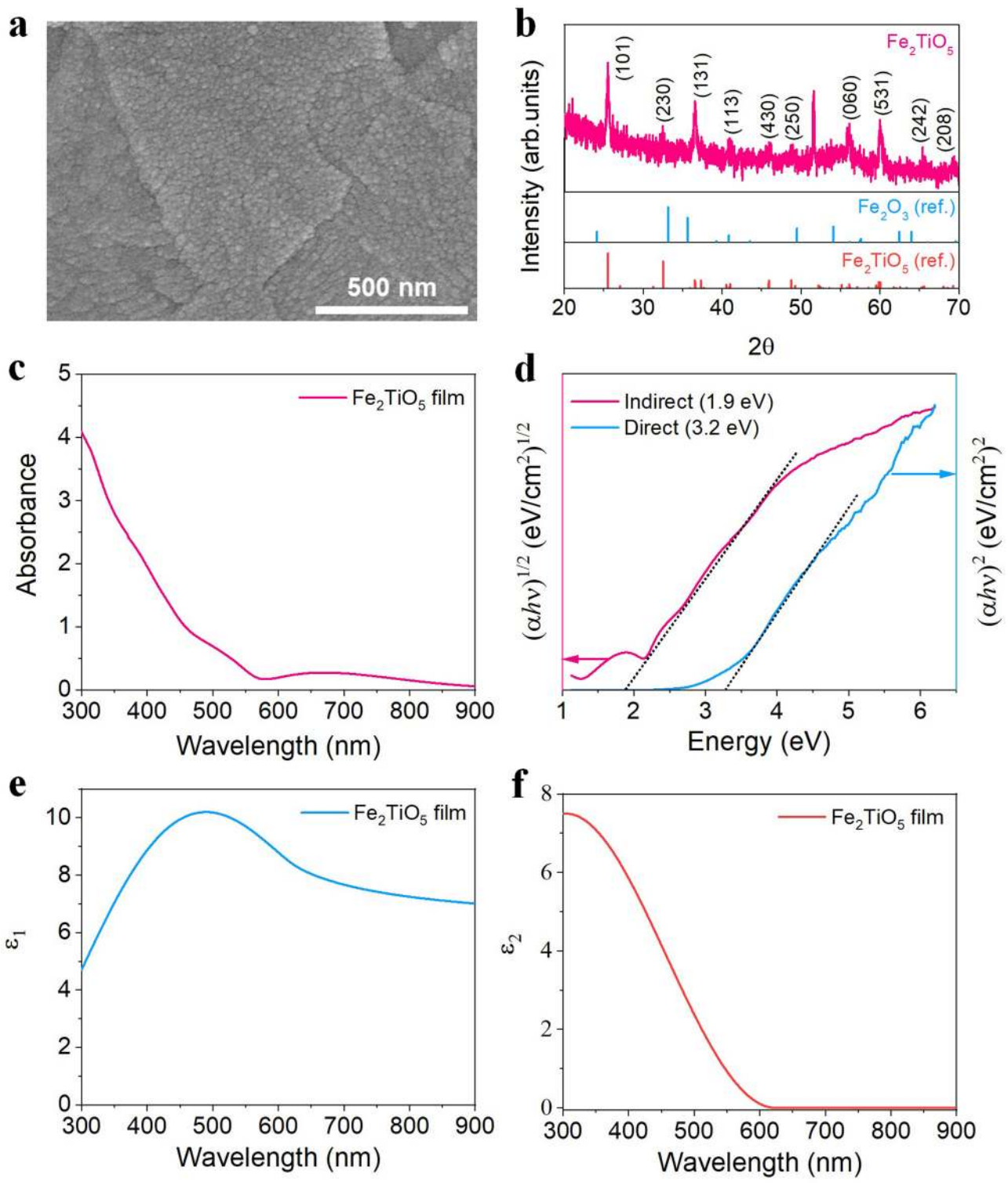

FIG. 1. (a)–(c) SEM image, XRD pattern, and absorbance spectra of the Fe_2TiO_5 thin film. (d) The Tauc plot generated from absorbance spectra of the Fe_2TiO_5 thin film. (e) Real and (f) imaginary parts of the dielectric function of the Fe_2TiO_5 thin film.

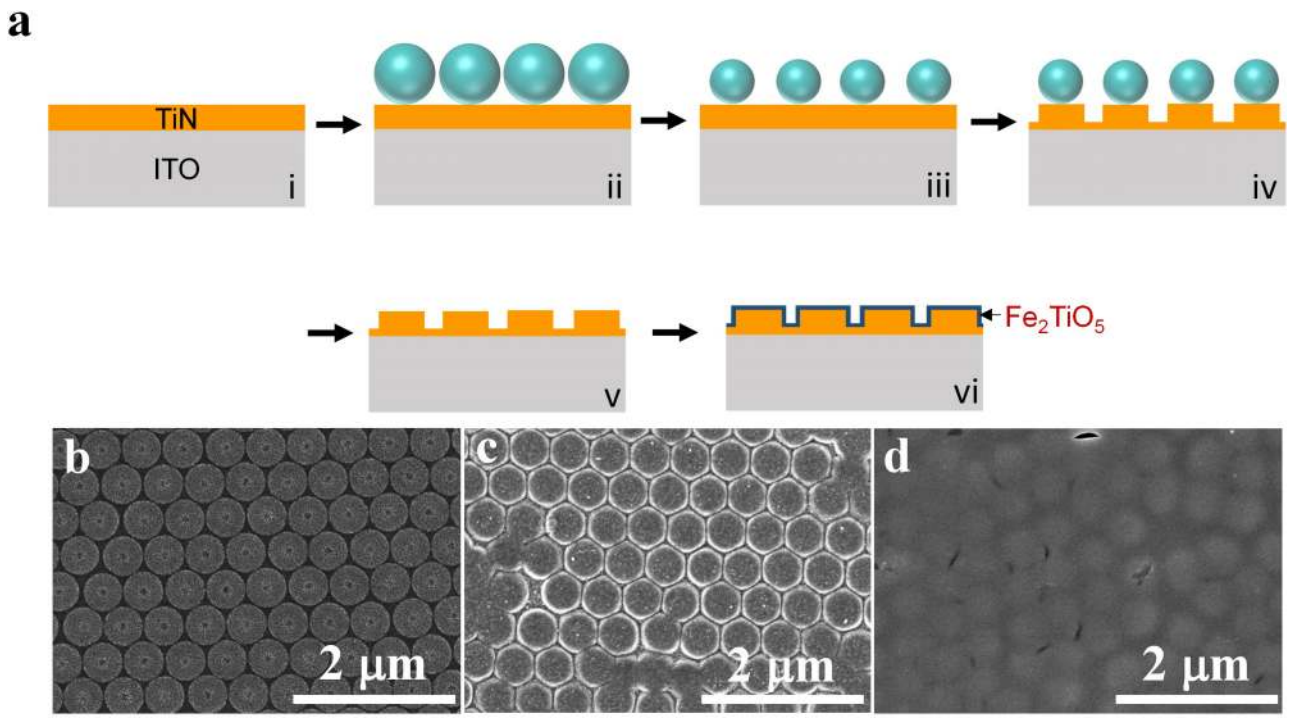

FIG. 2. (a) Illustration (not to scale) of the fabrication process of the nanodisk arrays. (b) SEM image of the TiN nanodisk arrays. (c) and (d) SEM images of the ITO/TiN/Fe_2TiO_5 and ITO/TiN/Cr-TiO_2 nanodisk arrays.

deviation in fitting the dielectric constants of the sputtered oxide thin films.

Figure 4(a) shows the photocurrent densities curves under the irradiation of artificial sunlight for planar ITO/Fe_2TiO_5, ITO/TiN/Fe_2TiO_5, and nanodisk arrays of ITO/TiN/Fe_2TiO_5 samples under a potential scan. Also, to study the performance of TiN/Fe_2TiO_5 compared with commonly studied plasmonic Au, ITO/Au/Fe_2TiO_5 planar sample was fabricated and its photocurrent density is also shown in Fig. 4(a). The ITO/TiN substrate does not show photoresponse. The Fe_2TiO_5 film shows ~4.5 and ~6.2 times larger photocurrent at 0.5 V vs Ag/AgCl reference, on planar and disk array of TiN substrates, respectively. Compared to the planar ITO/TiN/Fe_2TiO_5 sample, the disk array sample show ~1.4 times larger photocurrent. The planar ITO/TiN/Fe_2TiO_5 shows ~1.5 times larger photocurrent at 0.5 V vs Ag/AgCl, compared to ITO/Au/TiN sample. We further investigated this enhancement by measuring their wavelength-dependent photocurrent. All samples show strong photoresponse in the UV region and it decreases in longer wavelengths [Fig. 4(b)], which is very similar to the light absorption behavior of Fe_2TiO_5 film [Fig. 1(c)]. It can be clearly seen that the photocurrent density of Fe_2TiO_5 film is enhanced by ~26-fold and ~11-fold in the UV (<400 nm) and visible (400–750 nm) regions by making a hybrid structure with nanodisk arrays of TiN (ITO/TiN/Fe_2TiO_5). Also, the nanodisk arrays of ITO/TiN/Fe_2TiO_5 shows ~1.4-fold and ~threefold enhancement in UV and visible regions compared to the similar sample with a planar structure. The planar ITO/TiN/Fe_2TiO_5 sample shows ~15-fold and ~twofold enhancement in UV and visible regions compared to the similar sample made up with Au (ITO/Au/Fe_2TiO_5). For the case of ITO/Au/Fe_2TiO_5 planar sample [Fig. 3(a)], the absorption spectrum is similar to that of Fe_2TiO_5 film, which indicates limited absorption enhancement by Au. The photocurrent measurements suggest that the plasmonic TiN is more efficient than Au to enhance the photocurrent of Fe_2TiO_5, and by making its nanodisk arrays structures, the photocurrent generation can be improved further.

We further investigated their incident-photon-to-current efficiency (IPCE) as[43] IPCE (%) = $(1240 \times I_{sc})/(\lambda \times P_{in}) \times 100$, where I_{sc} is the photocurrent density (A cm^{-2}), P_{in} is the incident light power (W·cm^{-2}), and λ is the wavelength (nm). The IPCE spectra for all the samples are shown in Fig. 4(c). The major difference between all the samples lies in the UV regime (<450 nm), where the IPCE from the nanodisk arrays of ITO/TiN/Fe_2TiO_5 is significantly larger than that from other samples. In the visible region, the nanodisk arrays sample also shows higher IPCE than the other samples. The larger IPCE value of TiN/Fe_2TiO_5 observed here is likely due to the strong light absorption and efficient electron injection from the TiN to Fe_2TiO_5.

To observe the effect of Fe_2TiO_5 film thickness on photocurrent enhancement, we fabricated the planar sample of ITO/TiN/Fe_2TiO_5 with 40 and 80 nm thick Fe_2TiO_5 films. The 40 nm thick Fe_2TiO_5 film was observed to be discontinuous [Fig. S3(a) in the

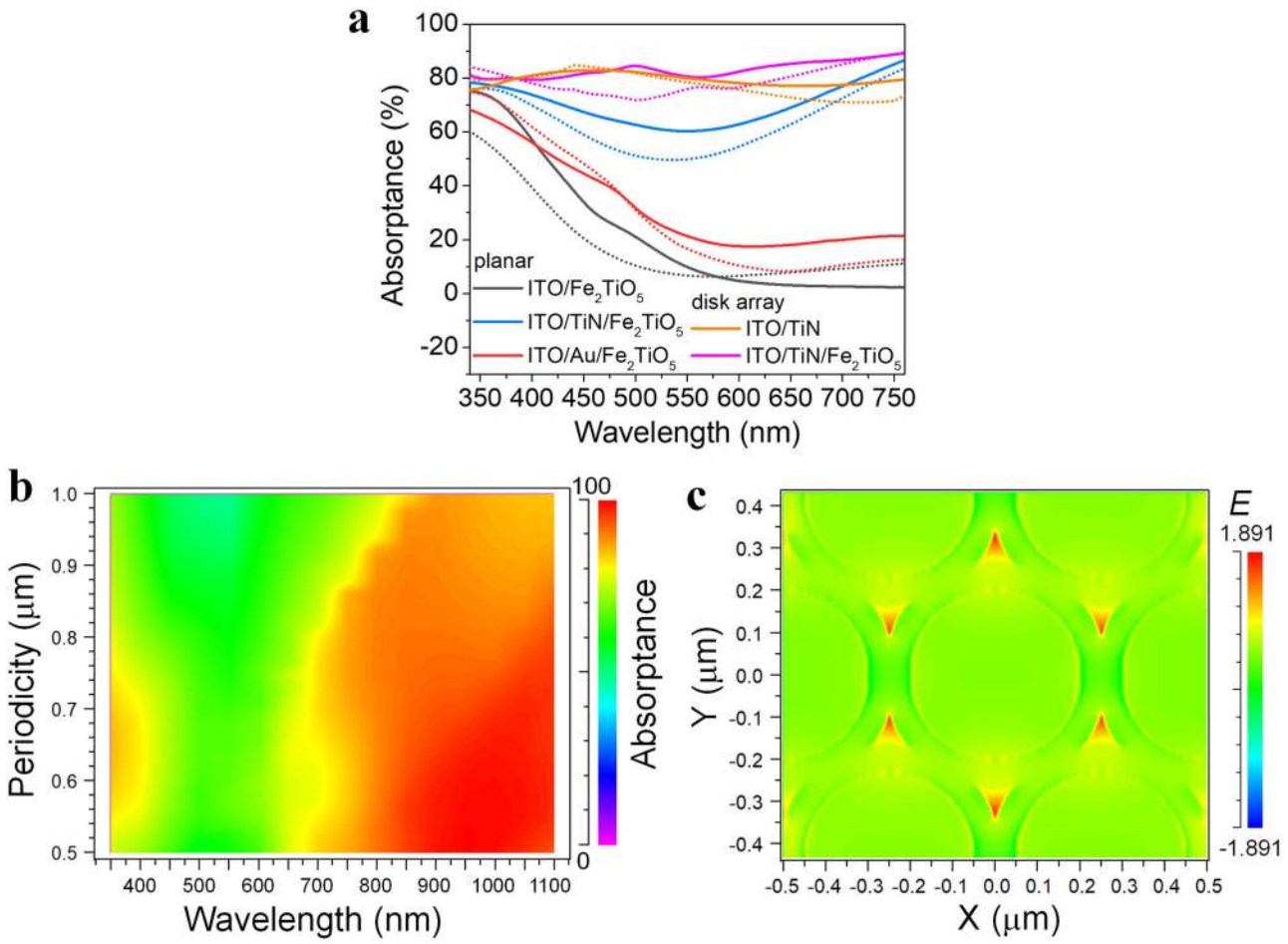

FIG. 3. (a) Experimental and calculated absorptance spectra of planar Fe_2TiO_5, TiN/Fe_2TiO_5, Au/Fe_2TiO_5 and nanodisk array of TiN and TiN/Fe_2TiO_5 on the ITO substrate. The experimental and calculated curves are shown in solid and dotted lines, respectively. (b) The relationship between the absorptance and the period for TiN/Fe_2TiO_5 nanodisk (disk diameter and height are 410 nm and 260 nm, respectively). (c) Electric field (X direction) mode profile at 900 nm for TiN/Fe_2TiO_5 nanodisk array for 500 nm disk period. The E-field is monitored in the XY plane placed at the top of the disks.

supplementary material], and the photocurrent was not observed due to the exposure of ITO/TiN to the electrolyte, which makes direct contact between both the electrodes. The 80 nm thick Fe_2TiO_5 film shows photoresponse (Fig. S4 in the supplementary material); however, it is smaller than the 60 nm thick Fe_2TiO_5 sample. As Fe_2TiO_5 has a short charge carrier diffusion length, the larger photocurrent is expected from the thinner film.

Next, ITO/TiN/Fe_2TiO_5 samples with 60 nm thick Fe_2TiO_5 film on different diameters of TiN nanodisks (270, 340 nm) with the height of 200 nm and periodicity of 500 nm were additionally fabricated [Figs. S3(b) and S3(c) in the supplementary material]. All the samples show strong and broad absorptance in the UV–Vis region [Fig. S5(a) in the supplementary material]. The 410 nm diameter of the nanodisk sample shows the strongest absorptance and largest photocurrent [Fig. S5(b) in the supplementary material] than the other samples. Overall, the 60 nm thick Fe_2TiO_5 film and 410 nm nanodisk diameter samples are observed to be the optimum combination among the conditions that were investigated. We believe that there is a room to further improve the photocurrent of TiN/Fe_2TiO_5 hybrid structure by optimizing the Fe_2TiO_5 thickness and geometry of plasmonic TiN structures for efficient light absorption and hot carrier transfer.

The planar and nanodisk array of TiN are observed to be effective in enhancing the photoresponse of Fe_2TiO_5. To investigate its effectiveness in enhancing the photoresponse of Cr-TiO_2, Fig. S6 in the supplementary material shows the photocurrent density of planar ITO/Cr-TiO_2, ITO/TiN/Cr-TiO_2, and disk array of ITO/TiN/Cr-TiO_2 samples under a potential scan irradiated by the artificial sunlight. The Cr-TiO_2 film shows ~1.7 and ~2.5 times larger photocurrent at 0.5 V vs Ag/AgCl reference than on planar and disk array of TiN substrates, respectively. Compared to the planar ITO/TiN/Cr-TiO_2 sample, the disk array sample shows

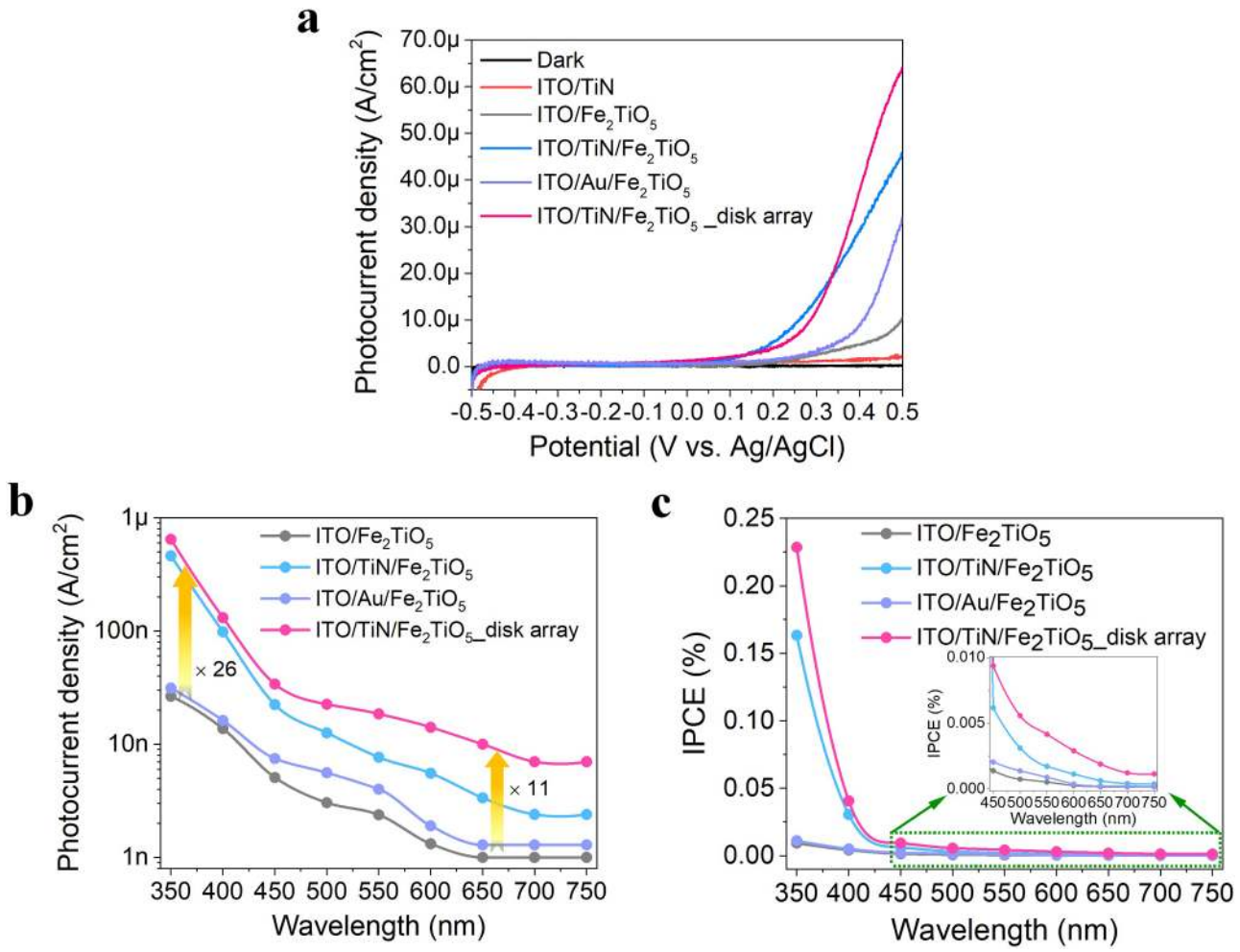

FIG. 4. (a) Anodic photocurrent under the irradiation of artificial sunlight. (b) Wavelength-dependent photocurrent density at zero bias, and (c) incident photon to current efficiency (IPCE) under different excitation wavelengths for planar ITO/Fe_2TiO_5, ITO/TiN/Fe_2TiO_5, ITO/Au/Fe_2TiO_5, and disk array of ITO/TiN/Fe_2TiO_5 samples.

~1.6 times larger photocurrent at 0.5 V. Figure 5(a) shows the photocurrent density of planar and nanodisk array of ITO/TiN/Cr-TiO_2 under the UV and visible light irradiation. The nanodisk array sample show ~18-fold and ~sixfold enhancement in the UV (<400 nm) and visible (400–750 nm) regions compared to the planar sample. Similar to the TiN/Fe_2TiO_5 samples, the TiN/Cr-TiO_2 planar and nanodisk array samples show broad and strong absorption in the UV–Vis region (Fig. S7 in the supplementary material). Broad and enhanced light absorption is clearly observed in Figs. 3(a) and S7 in the supplementary material due to the introduction of nanodisks. Next, the performance of ITO/TiN/Cr-TiO_2 samples were compared with respect to ITO/TiN/Fe_2TiO_5 samples. For the planar (nanodisk array) samples, compared to ITO/TiN/Cr-TiO_2, the ITO/TiN/Fe_2TiO_5 shows ~31-fold (~2.3-fold) and ~threefold (1.3-fold) enhancement in the UV and visible regions, respectively [Figs. 4(b) and 4(c) in the supplementary material]. Overall, for photocurrent generation, the hybrid structure of TiN with Fe_2TiO_5 is observed to be more efficient than with Cr-TiO_2.

In Fig. 6(a), we compared the enhancement factor, which is the ratio between the photocurrent from the nanodisk arrays and the planar films. For Fe_2TiO_5 and Cr-TiO_2 samples, the enhancements in the UV region are ~1.3 and ~22 times, and in the visible region, it is ~three and ~five times, respectively. Fe_2TiO_5 show larger enhancement in the visible region, while Cr-TiO_2 sample shows larger enhancement in the UV region.

To understand the mechanism of the enhanced photoresponse after the addition of TiN or Au, the band structures of TiN/Fe_2TiO_5, TiN/Cr-TiO_2, and Au/Fe_2TiO_5 under UV–Vis light illumination have been illustrated in Figs. 6(b) and S8 in the supplementary material, respectively. For Fe_2TiO_5 which is n-type, the photocurrent enhancement is caused by hot electrons transfer

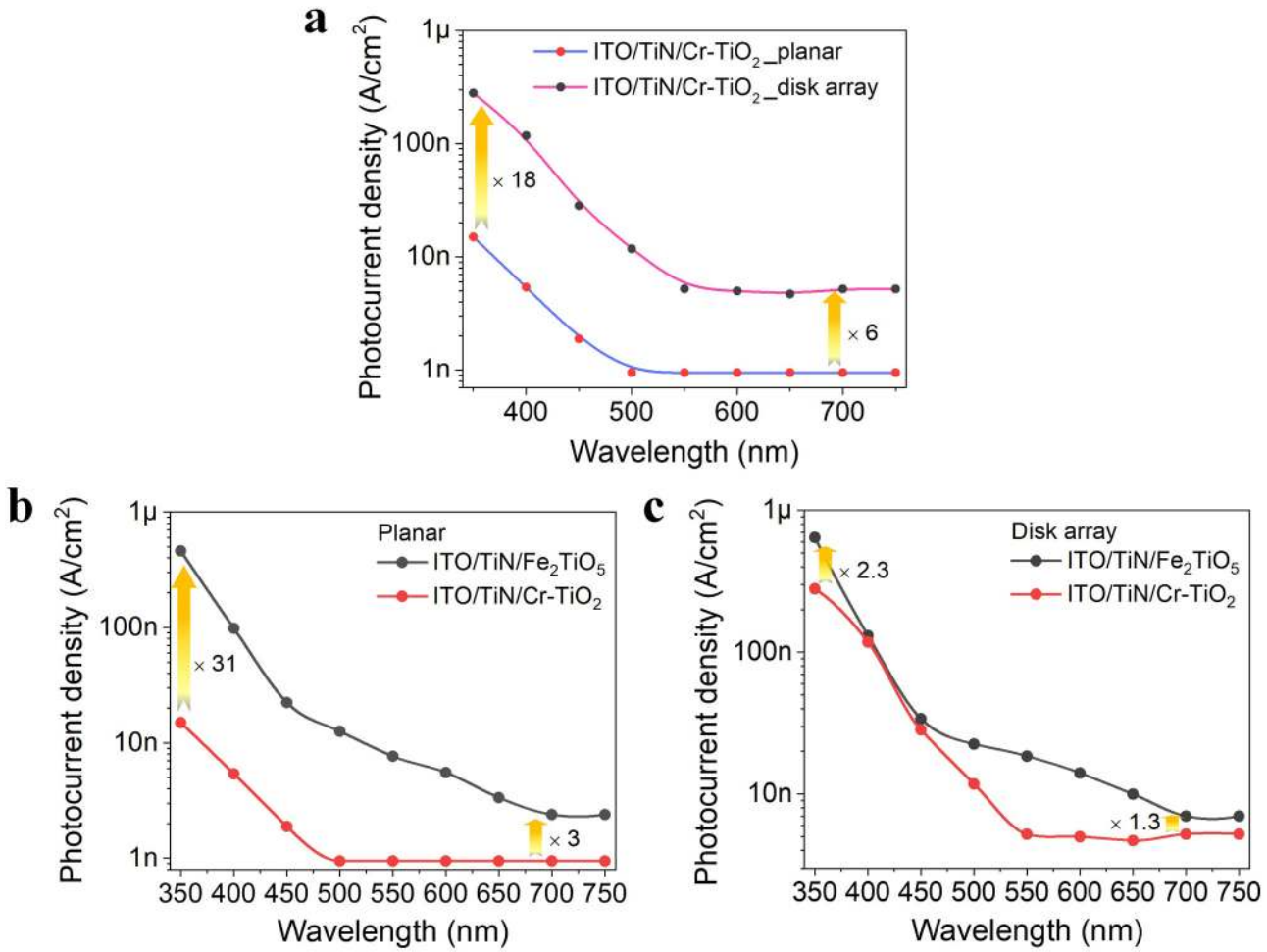

FIG. 5. (a) Photocurrent density of planar and nanodisk arrays samples of ITO/TiN/Cr-TiO_2. Comparison of (b) planar and (c) nanodisk array samples of ITO/TiN/Fe_2TiO_5 and ITO/TiN/Cr-TiO_2.

from TiN. The experimentally measured work function of TiN, bandgap of Fe_2TiO_5, and Fermi level of Fe_2TiO_5 are, respectively 4.6 eV, 1.9 eV, and 4.83 eV. As such, when Fe_2TiO_5 is deposited on TiN, it forms an ohmic contact at the interface. Thus, there is no barrier for electrons injection and also low energy hot electrons from TiN can be injected into Fe_2TiO_5 [Fig. 6(b)]. In particular, for the wavelengths that have smaller energy than the bandgap of Fe_2TiO_5, the excited hot electrons in TiN mainly contribute to photocurrent enhancement as shown in Fig. 4(b). In the case of the ITO/TiN/Cr-TiO_2 sample, a p-type Schottky barrier is formed where the expected barrier height is 2.8 eV. In the UV to green spectra, hot holes can be excited from TiN and transfer to the Cr-TiO_2 [Fig. 6(b)]. In longer wavelengths, the photon energy is not sufficient to excite the hot holes and transfer to Cr-TiO_2, thus its photoresponse is stronger in UV to green spectra and weaker in longer wavelengths [Fig. 6(a)]. Also, the energy band diagram for Au/Fe_2TiO_5 is shown in Fig. S8 in the supplementary material. Au and Fe_2TiO_5 form a barrier height of 0.8 eV. Due to the larger barrier height and lower absorptance, the photoresponse of Au/Fe_2TiO_5 is observed to be lower than the TiN/Fe_2TiO_5. Finally, we discuss the effect of surface area increase due to nanodisk array formation. The calculated surface area increase due to the formation of nanodisk array is roughly 2.3 times larger than the planer film area. However, photocurrent enhancements larger than 2.3 times are observed for both Fe_2TiO_5 and Cr-TiO_2. Thus, the photocurrent enhancements are not only due to the surface increase but also due to the increase in absorption by the nanodisk arrays and hot carrier transfer from the TiN to Fe_2TiO_5 or Cr-TiO_2.

In the case of a visible light-active photocatalyst, apart from an appropriate bandgap, the proper matching of the conduction band (CB) and valence band (VB) levels with the redox potentials of the photocatalytic reactions is extremely important for water splitting. A schematic diagram of the total water-splitting reaction using TiN/Fe_2TiO_5 and TiN/Cr-TiO_2 are shown in Fig. 6(b). The

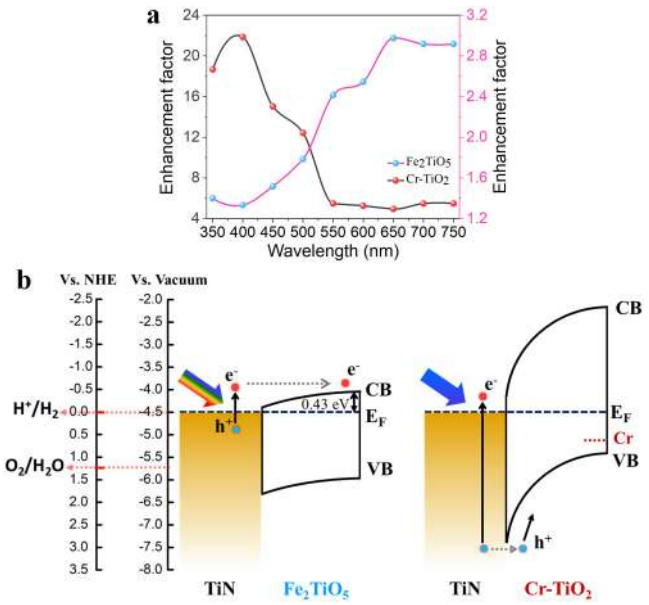

FIG. 6. (a) Photocurrent enhancement spectra for Fe_2TiO_5 and Cr-TiO_2, where enhancement was defined by taking the ratio of the nanodisk and film samples. For nanodisk array samples, the nanodisk diameters are 410 nm. (b) Schematic representation of the energy level band diagram at the Fermi level equilibrium for TiN/Fe_2TiO_5 and TiN/Cr-TiO_2, and standard redox potential of different oxidative species with respect to vacuum energy levels and NHE.

oxidation and reduction potential levels of water lie within the CB and VB potentials of Fe_2TiO_5 and Cr-TiO_2, which is suitable for an efficient charge transfer for electrochemical reactions and high efficiency in catalysis. Our proposed methodology of combining low-cost plasmonic TiN nanodisk array with earth-abundant oxides is a highly promising approach for designing efficient and cost-effective catalysts for photoelectrochemical conversion.

IV. CONCLUSION

In summary, we reported the broadband and strongly absorptive hybrid structure by using two titanate catalysts, n-type Fe_2TiO_5 and p-type Cr-TiO_2, in combination with TiN nanodisk arrays for enhanced PEC. The TiN nanodisk platform greatly improved the overall solar light absorption across a broad wavelength range, leading to huge photocurrent enhancement mediated by enhanced absorption and hot carrier transfer from TiN to Fe_2TiO_5 or to Cr-TiO_2. The photocurrent obtained with the hybrid structure of TiN/Fe_2TiO_5 nanodisk arrays was ~26-fold larger than that obtained with the bare Fe_2TiO_5 film. Similarly, the TiN nanodisk arrays enhance the photocurrent of Cr-TiO_2 by ~18-fold. Utilization of both hot electrons and hot holes from TiN indicates its suitability to combine with both n- and p-type oxides for PEC reactions. Overall, our proposed approach can be readily adopted for other photocatalytic semiconductors making them attractive for a wide range of applications based on solar energy harvesting. Further optimization and improvement of this synergistic effect is expected and could provide useful information towards designing visible photocatalysts for practical applications.

SUPPLEMENTARY MATERIAL

See the supplementary material for the table of sputtering conditions, schematic of the photoelectrochemical setup, experimental and calculated absorptance spectra, E-field map of the TiN disk array, SEM images of the Fe_2TiO_5 film, ITO/TiN/Fe_2TiO_5 disk arrays with different disk diameters, photocurrent density of the ITO/TiN/Fe_2TiO_5 planar sample with different thickness, experimental and calculated absorptance spectra of the ITO/TiN/Fe_2TiO_5 disk array with different diameters, anodic photocurrent, absorbance spectra of Cr-TiO_2 and TiN/Cr-TiO_2, and the schematic representation of the energy level band diagram for Au/Fe_2TiO_5.

ACKNOWLEDGMENTS

S.L.S., S.I., and T.N. acknowledge JSPS KAKENHI Grant Nos. 16K17496, 17H0480, and 16H06364, respectively. The authors thank Mr. Min-Wen Yu for his help in Kelvin force probe microscopy measurements.

DATA AVAILABILITY

The data that support the findings of this study are available within the article [and its supplementary material].

REFERENCES

[1]A. Kudo and Y. Miseki, Chem. Soc. Rev. **38**, 253 (2009).
[2]A. Paracchino, V. Laporte, K. Sivula, M. Grätzel, and E. Thimsen, Nat. Mater. **10**, 456 (2011).
[3]F. Opoku, K. K. Govender, C. G. C. E. van Sittert, and P. P. Govender, Adv. Sustain. Syst. **1**, 1700006 (2017).
[4]N. Serpone and A. V. Emeline, J. Phys. Chem. Lett. **3**, 673 (2012).
[5]Z.-F. Huang, J. Song, L. Pan, X. Zhang, L. Wang, and J.-J. Zou, Adv. Mater. **27**, 5309 (2015).
[6]S. Adhikari, D. Sarkar, and G. Madras, RSC Adv. **5**, 11895 (2015).
[7]Y. Gao, Y. Li, G. Yang, S. Li, N. Xiao, B. Xu, S. Liu, P. Qiu, S. Hao, and L. Ge, ACS Appl. Mater. Interfaces **10**, 39713 (2018).
[8]H.-C. Ho, K. Chen, T. Nagao, and C.-H. Hsueh, J. Phys. Chem. C **123**, 21103 (2019).
[9]S. Shen, S. A. Lindley, X. Chen, and J. Z. Zhang, Energ. Environ. Sci. **9**, 2744 (2016).
[10]F. Le Formal, M. Grätzel, and K. Sivula, Adv. Funct. Mater. **20**, 1099 (2010).
[11]J. Zhao, Y. Guo, L. Cai, H. Li, K. X. Wang, I. S. Cho, C. H. Lee, S. Fan, and X. Zheng, ACS Energy Lett. **1**, 68 (2016).
[12]A. Wolcott, W. A. Smith, T. R. Kuykendall, Y. Zhao, and J. Z. Zhang, Small **5**, 104 (2009).
[13]Z. Lin, C. Du, B. Yan, and G. Yang, Catal. Sci. Technol. **9**, 5582 (2019).
[14]M. Mishra and D.-M. Chun, Appl. Catal. A Gen. **498**, 126 (2015).
[15]J. Deng, X. Lv, and J. Zhong, J. Phys. Chem. C **122**, 29268 (2018).
[16]J. Deng, X. Lv, J. Liu, H. Zhang, K. Nie, C. Hong, J. Wang, X. Sun, J. Zhong, and S.-T. Lee, ACS Nano **9**, 5348 (2015).
[17]J. Deng, X. Lv, K. Nie, X. Lv, X. Sun, and J. Zhong, ACS Catal. **7**, 4062 (2017).
[18]K. Chen, T. D. Dao, T. D. Ngo, H. D. Ngo, A. Tamanai, S. Ishii, X. Li, H. Misawa, and T. Nagao, Nano Energy **76**, 104965 (2020).
[19]C. X. Kronawitter, L. Vayssieres, S. Shen, L. Guo, D. A. Wheeler, J. Z. Zhang, B. R. Antoun, and S. S. Mao, Energy Environ. Sci. **4**, 3889 (2011).
[20]S. Shen, P. Guo, D. A. Wheeler, J. Jiang, S. A. Lindley, C. X. Kronawitter, J. Z. Zhang, L. Guo, and S. S. Mao, Nanoscale **5**, 9867 (2013).

[21]R. P. Sugavaneshwar, K. Chen, G. Lakshminarayana, S. Ishii, T. D. Dao, N. Umezawa, and T. Nagao, APL Mater. **3**, 116103 (2015).
[22]T. D. Dao, G. Han, N. Arai, T. Nabatame, Y. Wada, C. V. Hoang, M. Aono, and T. Nagao, Phys. Chem. Chem. Phys. **17**, 7395 (2015).
[23]Y. Tian and T. Tatsuma, J. Am. Chem. Soc. **127**, 7632 (2005).
[24]C. Clavero, Nat. Photonics **8**, 95 (2014).
[25]Y. Fang, Y. Jiao, K. Xiong, R. Ogier, Z.-J. Yang, S. Gao, A. B. Dahlin, and M. Käll, Nano Lett. **15**, 4059 (2015).
[26]A. A. Hussain, B. Sharma, T. Barman, and A. R. Pal, ACS Appl. Mater. Interf. **8**, 4258 (2016).
[27]A. Naldoni, U. Guler, Z. Wang, M. Marelli, F. Malara, X. Meng, L. V. Besteiro, A. O. Govorov, A. V. Kildishev, A. Boltasseva, and V. M. Shalaev, Adv. Opt. Mater. **5**, 1601031 (2017).
[28]S. Ishii, S. L. Shinde, and T. Nagao, Adv. Opt. Mater. **7**, 1800603 (2019).
[29]S. Ishii, S. L. Shinde, W. Jevasuwan, N. Fukata, and T. Nagao, ACS Photonics **3**, 1552 (2016).
[30]M. Kaur, S. L. Shinde, S. Ishii, W. Jevasuwan, N. Fukata, M.-W. Yu, Y. Li, J. Ye, and T. Nagao, ACS Appl. Mater. Interf. **12**, 31327 (2020).
[31]S. L. Shinde, S. Ishii, T. D. Dao, R. P. Sugavaneshwar, T. Takei, K. K. Nanda, and T. Nagao, ACS Appl. Mater. Interf. **10**, 2460 (2018).
[32]S. L. Shinde, S. Ishii, and T. Nagao, ACS Appl. Mater. Interf. **11**, 21965 (2019).
[33]S. Rej, L. Mascaretti, E. Y. Santiago, O. Tomanec, S. Kment, Z. Wang, R. Zbořil, P. Fornasiero, A. O. Govorov, and A. Naldoni, ACS Catal. **10**, 5261 (2020).
[34]N. A. Güsken, A. Lauri, Y. Li, T. Matsui, B. Doiron, R. Bower, A. Regoutz, A. Mihai, P. K. Petrov, R. F. Oulton, L. F. Cohen, and S. A. Maier, ACS Photonics **6**, 953 (2019).
[35]S. Podder and A. R. Pal, Opt. Mater. **97**, 109379 (2019).
[36]B. Hou, L. Shen, H. Shi, R. Kapadia, and S. B. Cronin, Phys. Chem. Chem. Phys. **19**, 2877 (2017).
[37]Z. Lian, M. Sakamoto, H. Matsunaga, J. J. M. Vequizo, A. Yamakata, M. Haruta, H. Kurata, W. Ota, T. Sato, and T. Teranishi, Nat. Commun. **9**, 2314 (2018).
[38]Q. Sun, C. Zhang, W. Shao, and X. Li, ACS Omega **4**, 6020 (2019).
[39]K. Chen, B. B. Rajeeva, Z. Wu, M. Rukavina, T. D. Dao, S. Ishii, M. Aono, T. Nagao, and Y. Zheng, ACS Nano **9**, 6031 (2015).
[40]E. D. Palik, *Handbook of Optical Constants of Solids* (Elsevier, Amsterdam, 1998).
[41]H. D. Ngo, T. D. Ngo, A. Tamanai, K. Chen, N. T. Cuong, O. S. Handegard, A. Pucci, N. Umezawa, T. Nabatame, and T. Nagao, Cryst. Eng. Comm. **21**, 34 (2019).
[42]M. Thirumoorthi and J. Thomas Joseph Prakash, J. Asian Ceram. Soc. **4**, 124 (2016).
[43]Z. Chen, T. G. Deutsch, H. N. Dinh, K. Domen, K. Emery, A. J. Forman, N. Gaillard, R. Garland, C. Heske, T. F. Jaramillo, A. Kleiman-Shwarsctein, E. Miller, K. Takanabe, and J. Turner, *Photoelectrochemical Water Splitting: Standards, Experimental Methods, and Protocols* (Springer, New York, 2013), p. 87.